International Journal of Fatigue 209 (2026) 109602

Contents lists available at ScienceDirect

International Journal of Fatigue

journal homepage: www.elsevier.com/locate/ijfatigue

Experimental and FEM analysis of fatigue behavior of impact-damaged 7075-T6 aluminum components☆

Emanuele Vincenzo Arcieri [a,*], Sergio Baragetti [a], Željko Božić [b]

[a] Department of Management, Information and Production Engineering, University of Bergamo, Viale Marconi 5, Dalmine 24044, Italy
[b] Faculty of Mechanical Engineering and Naval Architecture, University of Zagreb, I. Lučića 5, Zagreb 10000, Croatia

ARTICLE INFO

Keywords:
Impact damage
Residual stresses
Notch effect
7075-T6
Experimental tests
Finite element analysis

ABSTRACT

This study investigates the fatigue strength of 7075-T6 aluminum hourglass specimens subjected to perpendicular impact loading via experimental tests and finite element analysis. In the experimental campaign, a single impact dent was created at the minimum cross-section of each specimen using steel spheres at nominal speeds of 75, 87.5, and 100 m/s. The damaged specimens were subsequently tested under an identical rotating bending moment amplitude across all impact conditions to assess their fatigue lives. The finite element study was conducted in two phases. In the first phase, the Johnson–Cook plasticity model was adopted to assess the post-impact stress–strain state, and the Johnson–Cook failure law was included to simulate potential damage during impact. In the second phase, stress evolution during rotating bending was assessed through a sequence of static finite element simulations performed on the impact-damaged specimens, accounting for the residual stresses induced by impact. Experimental results revealed that fatigue life is nearly constant across the tested impact speeds. Finite element analyses supported these observations and demonstrated that residual stresses significantly contribute to the total stress field in the specimens during cyclic loading. This work contributes to the understanding of the fatigue behavior of lightweight components with complex geometries subjected to impact damage.

1. Introduction

The damage of components caused by the impact of foreign objects, commonly referred to as Foreign Object Damage (FOD), is an unpredictable phenomenon that can occur in aerospace sector [1]. Impact damage induces the appearance of stress concentrations, residual stresses, and microcracking, which accelerate fatigue failure [2–5]. Fatigue is a material degradation process that occurs under cyclic or time-varying loads. Unlike static loading conditions, fatigue failure can occur even when the applied stresses are much lower than the material ultimate strength, due to the progressive accumulation of damage that leads to initiation and propagation of cracks until failure [6–9]. Since aerospace components often work under variable loading and are susceptible to impacts from foreign objects of various hardness, shape, and size, a comprehensive investigation is required to assess the influence of impact damage on structural integrity.

Damage induced by impact events has been extensively investigated in the literature. Xiaozhou et al. [10] proposed a mechanical model to predict the damage in composite plates generated by low-speed impacts which accurately assesses contact forces, absorbed energy, and delamination damage. Sun and Hallet [11] investigated low-speed impact damage of composite laminates using experimental tests at different scales and finite element models with 3D and 2D elements to reduce computational cost. Riccio et al. [12] proposed a global–local finite element approach to predict delamination growth and intra-laminar damage in composite laminates under impact loading. Chen et al. [13] studied the impact resistance of boride reinforced Ti-6Al-4V functionally graded materials. Zhu et al. [14] investigated impact damage on carbon fiber-reinforced aluminum laminates at different speeds and impact angles for various stacking sequences. Results showed that higher impact speeds increase deformation depth and energy absorption, while higher impact angles provide a larger contact area, suggesting that optimizing laminate curvature could mitigate impact damage. Zhang et al. [15] performed finite element analyses to assess the influence of speed on impact dent geometry and induced residual stresses in Ti-6Al-4V and AM355 steel blades. A similar study was conducted by Yin et al. [16], who considered Ti-6Al-4V, 2A12 aluminum alloy and Q235 steel

☆ This article is part of a special issue entitled: 'ECF24' published in International Journal of Fatigue.

* Corresponding author.
E-mail address: emanuelevincenzo.arcieri@unibg.it (E.V. Arcieri).

https://doi.org/10.1016/j.ijfatigue.2026.109602
Received 30 November 2025; Received in revised form 15 February 2026; Accepted 27 February 2026
Available online 3 March 2026

Nomenclature

$\dot{\varepsilon}_0$	Reference strain rate
$\dot{\varepsilon}_{eq}$	Strain rate
$\overline{D}$	Damage parameter
D_1, D_2, D_3, D_4, D_5	Johnson–Cook failure constants
F_y, F_z	Components of the force to simulate rotating bending
N_f	Number of cycles to failure
T^*	Normalized temperature
T_{melt}	Melting temperature
T_{ref}	Reference temperature
ε_{eq}	Equivalent plastic strain
ε_f	Fracture strain
η	Load amplification factor
σ^*	Stress triaxiality (σ_h/σ_{VM})
σ_h	Hydrostatic stress
σ_F	Nominal fatigue stress
σ_{VM}	Von Mises stress
σ_a	Stress amplitude
σ_{eq}	Equivalent stress
σ_m	Mean stress
A, B, C, n, m	Johnson–Cook plasticity constants
D	Diameter of the specimen at the gripping points
E	Young's modulus
FOD	Foreign object damage
L	Specimen length
R	Fillet radius
RP	Reference point
T	Material temperature
UTS	Ultimate tensile strength
YS	Yield strength
d	Minimum diameter of the specimen in the gauge section
s, t, h	Dent dimensions
ν	Poisson's ratio
ρ	Density
σ	Stress

as projectile materials. The influence of impact parameters was also experimentally studied in [17] for Ti-6Al-4V simulation blades and in [18] for flat specimens, where a spring-mass analytical model was proposed for FOD. Duò et al. [19] assessed the residual stresses induced by the impact of a steel cube via experimental and finite element analysis. Residual stresses after FOD on flat and aerofoil specimens were also investigated by Frankel et al. [20]. Since aeroengine blades work in high temperature environments, even the effect of temperature on impact damage was investigated through experimental tests and finite element analysis by Yang et al. [21].

The studies cited above have mainly focused on the characterization of impact-induced damage, but the scientific community has also extensively investigated the fatigue behavior of components after such damage. Nowell et al. [22] analyzed the effects of impact angle, leading edge radius, and blade wedge angle on the fatigue strength of blade-like specimens and found that impact dent depth has a significant influence on fatigue strength. They proposed a theoretical model based on the Kitagawa–Takahashi diagram to link the dent size with the fatigue strength of the damaged specimens. However, they observed discrepancies between experimental and theoretical results, which were attributed to the presence of compressive residual stresses in the proximity of the impact dent. The existence of a compressive region was also noticed by Arcieri et al. [23] for the perpendicular impact of a sphere at the minimum cross section of an hourglass specimen. The model presented in [22] was improved in [24] by integrating the contribution of compressive stresses in a simplified manner. Zhu et al. [25] observed the initiation and propagation behavior of small fatigue cracks from FOD dents in Ti-6Al-4V flat specimens. They found that cracks nucleated from the micronotches at the material pileup of dent rim and obtained lower crack growth rates with respect to naturally-initiated cracks due to cold working. Specimens were impacted with angles of 30°, 60° and 90° and the most marked reduction in fatigue strength occurred for the intermediate impact angle, as a consequence of the generated impact dent geometry. Ding et al. experimentally investigated small crack growth behaviour in Ti-6Al-4V plate specimens after FOD under fatigue loading in [26] and proposed a fracture mechanics predictive model in [27]. A model to predict the fatigue strength of Ti-6Al-4V specimens damaged at different impact speed angles has also been proposed by Yin et al. [28]. The combined effects of impact damage and corrosion on steel components has been studied in [29].

Since many aerospace components susceptible to impact damage are manufactured from aluminum alloys, understanding their mechanical and fatigue behavior is of particular interest. Aluminum and its alloys are among the most widely used materials in aerospace engineering due to their low density and promising mechanical properties [30]. In aerospace, aluminum alloys offer high application potential compared to steels and even titanium, due to significantly lower production costs. Although titanium alloys are preferred for their superior mechanical properties and high-temperature performance [31,32], aluminum alloys can reduce weight by 25–40% compared to steel. In commercial aircraft, aluminum alloy components represent approximately 60–80% of total weight, with series 2xxx, 7xxx and Al-Li alloys being the most commonly used [33].

The literature studies on impact damage mainly focus on flat and airfoil geometries, whereas more complex geometries have only been marginally explored. For this reason, the authors of this paper have investigated impact damage in hourglass-shaped specimens made of 7075-T6 aluminum alloy and its implications on fatigue strength in previous studies [23,34–39]. In [34], residual stresses were modeled for perpendicular and oblique impacts and stress concentration effects were assessed in a simplified manner. Arcieri et al. [35,36] combined finite element modelling and experimental testing to understand the failure mechanism in a 7075-T6 specimen subjected to an impact event and subsequent fatigue loading. The observation of the fracture surface of the impact-damaged specimen revealed that cracks nucleated at the locations where the maximum axial tensile residual stress occurs over fatigue cycle. These nucleation sites coincide with the position of the highest tensile residual stresses [23]. The reduction in fatigue strength was interpreted using the Haigh (modified Goodman) diagram in [35]. The influences of impact speed, angle, and projectile material and dimension on the residual stresses after impact and on the stress state under rotating bending were studied via finite element analyses respectively in [37] and [38]. Results highlighted the dominant role of impact speed, followed by projectile material and size, and indicated that lower speeds and projectile masses induce smaller tensile residual stresses, as they generate lower impact forces and consequently shallower notches. In [39], the relationship between impact speed and notch depth was quantified via simplified finite element analyses. However, the previous analyses from the authors relied on finite element models based on elastic–perfectly plastic material behavior, which neglect the strain-rate dependency of material strength. Moreover, the influence of impact speed was assessed only numerically, without experimental validation. The present work overcomes these limitations by combining experimental impact tests at different speed with a finite element framework based on the Johnson–Cook plasticity and failure laws, enabling a more realistic description of impact phenomena and of the

resulting residual stress fields. The study analyzes the fatigue strength of 7075-T6 aluminum specimens subjected to the perpendicular impact of a steel sphere, with the impacts occurring at the minimum cross section [40]. In the experimental tests, impact dents were introduced using steel spheres at nominal speeds of 75, 87.5, and 100 m/s, where "nominal speed" refers to the theoretical speed derived from the air-gun setup used for shooting the steel spheres. The damaged specimens were then tested under an identical rotating bending moment amplitude to determine their fatigue lives. The finite element analysis employed the Johnson–Cook plasticity model to reproduce the post-impact stress–-strain state, and included the Johnson–Cook failure law to capture potential damage during the impact event. Stress evolution under rotating bending was subsequently assessed through a sequence of static finite element analyses performed on the impact-damaged specimens, accounting for the residual stresses induced by impact. Experimental findings indicate that fatigue life does not vary significantly across the tested impact speeds and finite element analyses confirmed the absence of marked differences in the stress distributions of the various impact-damaged specimens during fatigue loading.

2. Materials and methods

2.1. Experimental impact and rotating bending fatigue tests

7075-T6 aluminum alloy specimens were used for the experimental tests. Alloys from the 7000 series are known for their high mechanical strength and excellent strength-to-weight ratio, ideal for aerospace applications. Although their corrosion resistance is relatively lower compared to other aluminum series, this limitation can be mitigated through targeted thermal treatments [41]. The "T6" designation refers to a two-step heat treatment, typically consisting of solution heat treatment at 470°C for 3 h followed by water quenching at 20°C and artificial aging at 137°C for 12 h with slow air cooling [42]. Table 1 presents the chemical composition [43]. The specimens were designed according to ISO 1143 [44] with the shape shown in Fig. 1.

The impact bench of Fig. 2 was used to create impact dents on the specimens. The setup consists of an air gun system that uses compressed air to shoot 5 mm diameter steel spheres with a hardness of HRC40. Two pressure multipliers arranged in series enable the system to reach air pressures of up to 20 bar. Sphere speed is measured using two OMRON-E3XNA11 fiber optic amplifiers connected to a Tektronix TBS1102C oscilloscope. Each amplifier is connected to a pair of transmitting and receiving optical fibers that face each other, forming an optical measurement point. The two measurement points are aligned along the projectile trajectory and spaced 40 mm apart. The oscilloscope records the time interval between the signals generated at the two points, allowing the sphere speed to be calculated under the assumption of constant speed. A guide aligned with the barrel axis ensures accurate positioning of the specimen holder. Specimens are fixed using set screws and the holder is placed as close as possible to the barrel exit to minimize trajectory deviation and reduce air resistance effects.

Before the experimental impact test, the specimens were polished using abrasive paper with increasing grit sizes, from P400 to P4800. This procedure typically produces a nearly mirror-like finish, with an average surface roughness below 0.2 μm. No additional polishing steps were performed beyond this abrasive sequence. However, the influence of surface roughness on the fatigue behaviour of the impact-damaged specimens is expected to be negligible. The characteristic dimensions of the impact dents are much higher than the surface roughness, and

Table 1
Chemical composition of 7075-T6 [43].

Al [%]	Zn [%]	Mg [%]	Cu [%]	Fe [%]	Si [%]	Cr [%]	Mn [%]	Ti [%]
Balanced	5.6	2.55	1.75	0.32	0.25	0.22	0.20	0.12

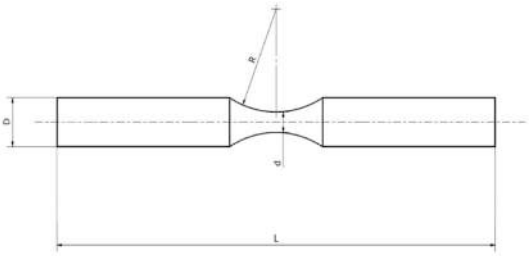

L [mm]	d [mm]	D [mm]	R [mm]
120	5	12	25

Fig. 1. Nominal dimensions of hourglass specimens.

therefore dominate the local stress field. The highest tensile residual stresses and the most severe stress concentrations typically occur in the vicinity of the impact damage, not in the undamaged polished regions. Consequently, crack nucleation is not expected to be driven by surface finishing quality, but rather by the residual stress state and geometric stress concentrations introduced by the impact event. Each specimen was subjected to a single impact, applied perpendicularly to its external surface at the minimum cross section. A total of nine specimens were tested, divided into three groups corresponding to firing pressure levels of 5, 7.5 and 10 bar, which were found to result in impact speeds of approximately 75 m/s, 87.5 m/s and 100 m/s, respectively, as described later.

Fatigue tests were conducted using an Italsigma RB35 rotating bending testing machine. An identical bending moment was applied to all the nine specimens and the number of cycles to failure was counted. The aim was to assess the fatigue life corresponding to a nominal applied rotating bending stress σ_F, where "nominal stress" refers to the stress that would be experienced by an undamaged specimen. The nominal stress σ_F was calculated as follows (Equation (1)):

$$\sigma_F = \sigma_{FAf,Al} \bullet \eta = 0.33 \bullet UTS \bullet \eta \tag{1}$$

where $\sigma_{FAf,Al}$ is the bending fatigue limit under fully reversed loading, assumed for a fatigue life of 2,000,000 loading cycles, and η is a load amplification factor. It should be noted that aluminium alloys do not exhibit a true fatigue limit; therefore, the value at 2,000,000 cycles was adopted in this study as a reference fatigue strength for determining the nominal bending stress to be applied. The fatigue limit was assumed equal to 0.33 times the material ultimate tensile strength UTS, based on [45]. The load amplification factor was introduced solely to increase the nominal bending stress above the conventional fatigue strength reference value, thus defining a higher stress level for the fatigue-life assessment of the impacted specimens and ensuring that the applied nominal stress would lead to lower fatigue lives. The combination of this increased nominal stress, tensile residual stresses induced by the impacts, and the notch-like geometry of the dents ensures that failure occurs within a number of cycles lower than 2,000,000. By assuming $\eta = 1.2$, a nominal stress of approximately 260 MPa was obtained, corresponding to a bending moment of 3.2 Nm, which was applied to all tested specimens.

The rotating bending tests were conducted at a constant speed of 2500 rpm, corresponding to a frequency of approximately 42 Hz. This value was selected based on the authors' previous experience with rotating bending tests on undamaged 7075-T6 specimens with the same geometry, both uncoated and DLC-coated [43], and ensures that excessive heating is avoided, preventing any alteration of the material's mechanical properties. The applied frequency is far below the minimum critical frequency, and to verify this aspect, a modal analysis was performed in Abaqus [46], following an approach consistent with the model described in Section 2.2 for assessing stress evolution over fatigue cycles. A material density of 2810 kg/m^3 was assigned to the aluminum

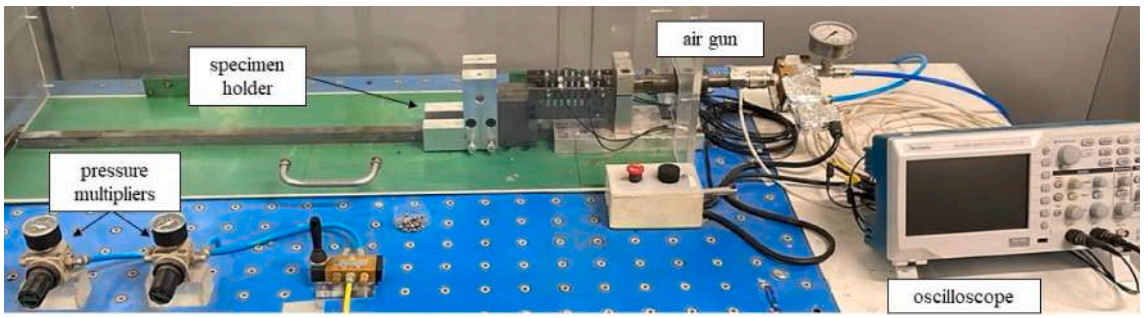

Fig. 2. Impact test bench.

alloy, and the Lanczos eigensolver algorithm was employed. The analysis was carried out on the specimen damaged at 100 m/s, importing the corresponding geometry and residual stress field. The first non-rigid natural frequency obtained was about 760 Hz, which is nearly twenty times higher than the applied rotation frequency. A simplified analytical estimate of the first critical frequency, obtained by modelling the specimen as a uniform bar with a diameter of 5 mm and a length equal to the full specimen, yields a value of approximately 690 Hz. This estimate is conservative, as it neglects the additional bending stiffness provided by the hourglass geometry. Therefore, resonance phenomena are not expected during the rotating bending fatigue tests. Furthermore, as the dimensions of the specimens are small, the selected rotation speed induces radial and circumferential stresses of only a few MPa, as predicted by the classical rotating-disk theory. Their contribution is therefore negligible compared with both the impact-induced stress field and the stresses generated during rotating bending.

The digital optical microscope Keyence VHX-7000 was employed to measure the dimensions of the impact dents and to acquire images of the fracture surfaces resulting from rotating bending fatigue tests.

2.2. Finite element analyses for the stress–strain state after impact and for the stress distribution under rotating bending

As in previous studies [23,34–39], Abaqus Explicit finite element code [46] was used to simulate the perpendicular impacts of a sphere on the hourglass specimens at their minimum cross section and to assess the resulting stress distributions. Three simulations were performed, differing only in the speed of the impacting sphere: 75 m/s, 87.5 m/s and 100 m/s. These values correspond to the nominal speeds associated with the firing pressures adopted in the experimental study. Due to both geometric and loading symmetry, only half of the specimen was modeled in order to reduce computational cost, Fig. 3. The whole sphere

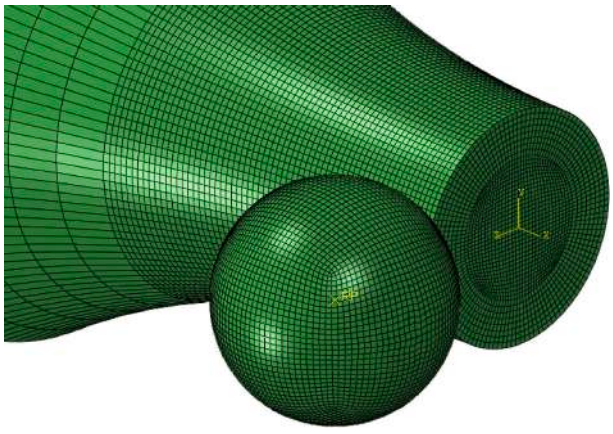

Fig. 3. Finite element model for impact simulation (based on [23,34–39]): detail of the mesh in the impact region.

was positioned with a 0.1 mm gap between its surface and that of the specimen along the impact direction to reduce computation time prior to contact. The specimen was assumed deformable while the sphere was defined as a rigid body. The Young's modulus of the steel sphere is approximately three times higher than the elastic modulus of the aluminum specimen and for this reason the deformation of the sphere can be considered negligible under the considered impact conditions. A Reference Point (RP) was assigned at the sphere's center.

Since the sphere was modeled as a discrete rigid body, no material properties were assigned, and only its mass of 0.51 g and corresponding moments of inertia were specified. To reproduce the post-impact stress–strain state in the damaged specimens, the plastic behavior of the aluminum alloy was modelled with the Johnson–Cook plasticity law, which accounts for strain, strain rate and temperature effects. The equivalent stress is expressed according to Equation (2) [47,48]:

$$\sigma_{eq} = \left(A + B\varepsilon_{eq}^{n}\right)\left(1 + C\ln\dot{\varepsilon}_{eq}^{*}\right)\left(1 - T^{*m}\right)$$
$$\dot{\varepsilon}_{eq}^{*} = \frac{\dot{\varepsilon}_{eq}}{\dot{\varepsilon}_{0}} \tag{2}$$
$$T^{*} = \frac{T - T_{ref}}{T_{melt} - T_{ref}}$$

where σ_{eq} is the equivalent stress; ε_{eq} is the equivalent plastic strain; $\dot{\varepsilon}_{eq}$ is the strain rate; $\dot{\varepsilon}_0$ is the reference strain rate; T is the material temperature; T_{ref} is the reference temperature; T_{melt} is the melting temperature; A, B, C, n are material constants.

In the finite element model, the Johnson–Cook failure law was included to capture potential damage during the impact event. Material failure was modeled using the Johnson–Cook failure criterion, which introduces a damage parameter $\overline{D}$ defined as reported in Equation (3) [49]:

$$\overline{D} = \sum \frac{\Delta\varepsilon_{eq}}{\varepsilon_{f}} \tag{3}$$

where $\Delta\varepsilon_{eq}$ is the increment of equivalent plastic strain in a deformation step and ε_f represents the equivalent plastic strain at fracture. Material failure is assumed to occur when $\overline{D}$ reaches a value of 1. Fracture strain ε_f is given by Equation (4):

$$\varepsilon_{f} = \left(D_1 + D_2 e^{D_3\sigma^{*}}\right)\left(1 + D_4 \ln\dot{\varepsilon}_{eq}^{*}\right)\left(1 + D_5 T^{*}\right) \tag{4}$$

where σ^* is the stress triaxiality, defined as the ratio between the hydrostatic stress σ_h and the equivalent stress σ_{eq}. In the model, σ_{eq} can be assumed equal to the von Mises stress σ_{VM}. Parameters D_1, D_2 and D_3 are determined by fitting equivalent plastic strain curves as a function of stress triaxiality. Similarly, D_4 and D_5 are determined by fitting equivalent plastic strain curves as a function of strain rate and temperature, respectively. In this study, thermal effects were excluded, setting $D_5 = 0$. Table 2 reports the material properties defined for the 7075-T6 specimens [23,48].

Table 2
Material properties for the 7075-T6 specimens [23,48].

Parameters	Values
Density ρ [g/cm^3]	2.81
Young's modulus E [MPa]	71,700
Poisson's ratio ν	0.33
Johnson–Cook plasticity constant A [MPa]	546
Johnson–Cook plasticity constant B [MPa]	678
Johnson–Cook plasticity constant n	0.71
Johnson–Cook plasticity constant C	0.024
Johnson–Cook plasticity constant m	1.56
Reference strain rate for plasticity $\dot{\varepsilon}_0$ [s^{-1}]	0.0005
Reference temperature T_{ref} [K]	293
Melting temperature T_{melt} [K]	893
Johnson–Cook failure constant D_1	−0.068
Johnson–Cook failure constant D_2	0.451
Johnson–Cook failure constant D_3	−0.952
Johnson–Cook failure constant D_4	0.036
Reference strain rate for failure $\dot{\varepsilon}_0$ [s^{-1}]	1

A dynamic explicit step was defined with a time of 15 ms since stress values appeared to reach a steady state within this time, showing no significant variation. Nonlinear geometric effects were included to improve accuracy under large deformation conditions.

Contact between the sphere and specimen was modeled using surface-to-surface explicit contact with a penalty-based constraint enforcement method. Normal contact behavior was set to "Hard contact" to prevent penetration and tangential behavior was modeled with a friction coefficient of 0.47 [50].

The impact speed (75, 87.5 or 100 m/s) was assigned to the RP at the center of the sphere, which was constrained to move only along the impact direction. To replicate the experimental conditions, the regions of the specimen corresponding to the fixture areas were fixed. Symmetry boundary conditions were applied on the minimum cross section of the hourglass specimen. As stated at the beginning of this section, the full sphere and only half of the specimen were modeled to reduce computational cost, due to the geometric and loading symmetry of the investigated impact phenomenon. The number of finite elements associated with the sphere is very small compared to the total number of elements in the model, and therefore the computational saving achievable by modeling only half of it would be negligible. Moreover, since the sphere was defined as a rigid body, it could not undergo any deformation and its contribution to the overall computational cost is minimal. The symmetry boundary condition applied on the minimum cross-section of the specimen, combined with the boundary conditions assigned to the RP of the impacting sphere, ensures that the results are identical to those obtained using a model with the full specimen and the full sphere, or a model with half of the specimen and half of the sphere under symmetry boundary conditions. For this reason, modeling the complete sphere together with half of the hourglass specimen does not affect the accuracy of the simulation.

The finite elements used for the hourglass specimen were C3D8R elements, which are 8-node linear hexahedral elements with reduced integration and hourglass control. The mesh was refined in the impact zone with an element size of 0.13 mm. The sphere was meshed with R3D4 elements, that are bilinear rigid quadrilateral elements with four nodes, using the same mesh size. This configuration provided sufficient accuracy in the high-gradient zone around the impact, while maintaining computational efficiency across the model. A mesh convergence test was performed for the 75 m/s impact simulation by comparing the results obtained with element sizes of 0.20 mm and 0.13 mm in the region where impact damage develops. The final mesh size was selected because further refinement would not lead to meaningful changes in displacement, von Mises stress, and axial stress after impact. The mesh was designed to be as close as possible to a structured grid, ensuring numerical robustness and avoiding excessively small elements. Since the impact simulations were carried out using an explicit solver, an excessively refined mesh would have significantly reduced the stable time increment, resulting in a substantial increase in computational time. The adopted mesh therefore represents a balanced choice between accuracy, numerical stability, and computational efficiency. The analyses were performed on two processors.

Another finite element model was developed to assess the evolution of the stresses under rotating bending, Fig. 4. To simulate the loading condition without significantly increasing computational cost, a sequence of static steps with a rotating force was created, following the approach adopted in the authors' previous works [35,36,38]. This approach is suitable because dynamic effects are negligible, and including them would have substantially increased computational cost without improving the accuracy of the stress analysis. The fatigue cycle simulation was performed for each impact speed condition, i.e., 75, 87.5 and 100 m/s. For each impact case, the corresponding damaged specimen mesh was imported, along with its residual stress distribution. The objective of this second finite element analysis was not to predict the number of cycles to failure, but to evaluate the stress evolution in the impact-damaged specimens during the early stages of cyclic loading, in order to understand how the induced residual stress field and stress concentrators interact with the applied bending stresses.

Material behavior in the rotating bending simulation was modified with respect to impact simulation by removing damage modeling. The Johnson–Cook failure law was not included because this could not adequately describe fatigue mechanisms, as shown in [51], and the rotating bending analysis was carried out using a classical stress-based approach. The boundary conditions were defined to reproduce a classical four-point bending configuration, consistent with the experimental setup. A kinematic coupling constraint was employed to rigidly constrain the motion of each node at the specimen end to the motion of the reference point RP-2, located at its center (Fig. 4). Similarly, the motion of each node along the perimeter of the cross-section located 22.5 mm from the minimum specimen section was constrained to the motion of RP-3, positioned at the center of the section. RP-2 was constrained against translation in the plane perpendicular to the specimen axis and against rotation about this axis. Symmetry boundary conditions were imposed at the minimum cross section of the specimen. To simulate the application of the rotating bending moment, a concentrated force was applied at RP-3. The force has two mutually perpendicular components, F_y and F_z, whose magnitudes were set to vary sinusoidally with a phase shift of 90° in order to produce a constant force magnitude throughout the simulated cycle. The simulation was extended to two complete cycles, with discrete increments of 9°. More than one cycle was included to verify whether local material yielding occurred as a consequence of the applied load. Geometric nonlinearity was accounted for in the analyses, which were performed on two processors.

3. Results and discussion

3.1. Impact dent dimensions from experimental tests and finite element analyses

Table 3 reports the impact speeds measured for the three nominal pressure levels adopted in the experimental tests and the impact dent dimensions obtained from experimental tests and finite element simulations. For the investigated pressure range, a linear relationship between the impact speed and the firing pressure can be assumed, as the coefficient of determination R^2 is very close to 1, Fig. 5. The consistency of the three repeated measurements performed at each pressure level could, in principle, be assessed using the Grubbs outlier test with a significance level of 0.05, even though the sample size is small and the statistical power is therefore limited. If such a test were conducted, the calculated statistics would remain below the corresponding critical threshold for all pressure levels, indicating that no statistically significant outliers would be present.

Due to the hourglass geometry of the tested specimens, the impact

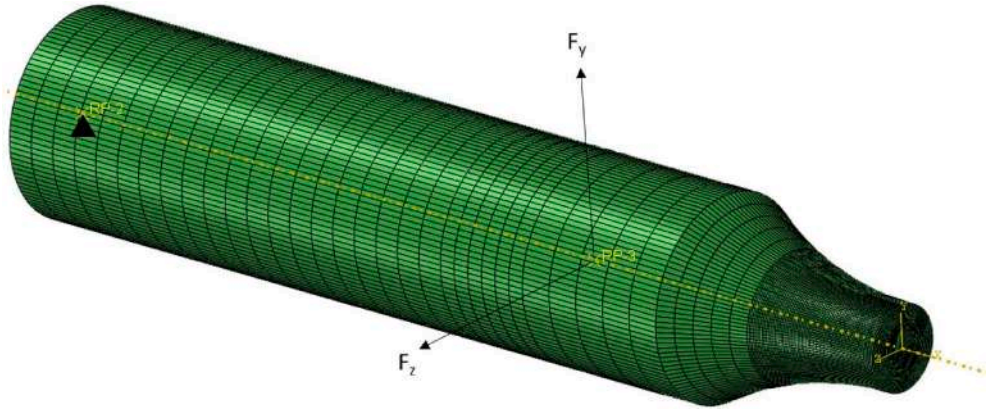

Fig. 4. Finite element model for rotating bending (based on [35,36,38]).

Table 3
Measured impact speeds and impact dent dimensions from experimental tests and finite element analyses.

Specimen	Pressure [bar]	Nominal impact speed [m/s]	Measured impact speed [m/s]	Experimental dent dimensions			Finite element dent dimensions		
				s [mm]	t [mm]	h [mm]	s [mm]	t [mm]	h [mm]
1	5	75	75.66	1.89	2.21	0.23	1.71	2.60	0.30
2			72.39	1.81	2.30	0.24			
3			75.09	1.88	2.36	0.20			
4	7.5	87.5	86.34	2.02	2.58	0.33	1.92	2.86	0.37
5			95.51	2.10	2.60	0.35			
6			88.59	2.06	2.59	0.29			
7	10	100	102.64	2.21	2.73	0.39	2.02	2.95	0.45
8			102.46	2.19	2.77	0.36			
9			101.96	2.24	2.70	0.35			

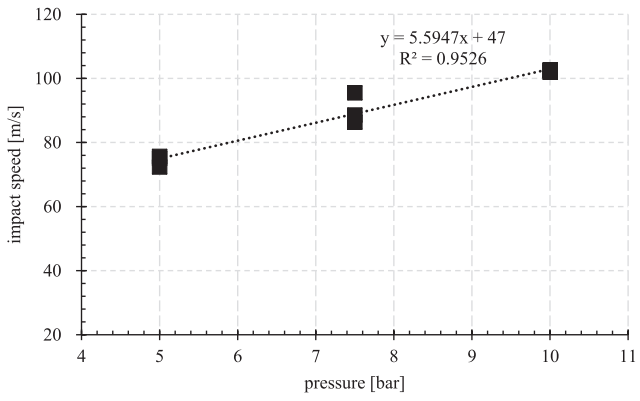

Fig. 5. Impact speed versus pressure diagram.

zone exhibits two distinct curvatures, one in the plane containing the specimen axis and the radial direction, and the other in the plane of the minimum cross-section. This geometric configuration requires three dimensions to fully characterize the dent geometry. Fig. 6a illustrates the definition of the three dimensions s, t and h. Fig. 6b-l show the experimentally obtained dent profiles for the nine specimens and report the corresponding measured values of the depth parameter h. The measurements of s and t are provided in the Appendix. Fig. 6m-o report the dent geometries obtained at the end of the finite element impact simulations, displayed using displacement-magnitude contour plots. In subfigures b–l, the color scale ranges from blue to red, with red indicating the points located at the highest positions relative to the reference plane and blue corresponding to the points at the lowest positions. In subfigures m–o, the colors again range from red to blue, but here red highlights the regions that experience the largest displacement in magnitude, whereas blue marks the undeformed areas. The identified trends of dent dimensions versus impact speed, derived from both experimental tests and finite element analyses, are shown in Fig. 7. The trend lines for both datasets were forced to pass through the origin of the diagram, reflecting the physical condition that dent dimensions are zero in the absence of impact events. The equation of the trend lines and the corresponding coefficients of determination R^2 are reported on the right side of the diagram. All the obtained R^2 values are higher than 0.99, indicating an excellent fit to the linear model. To quantify the discrepancy between experimental and finite element results, the comparison was performed on the slope of each trend line. Finite element analysis was found to overestimate the dent dimension s by approximately 7%, t by about 12% and h by roughly 23% with respect to experimental measurements. These discrepancies are acceptable and are likely due to the low probability of achieving perfectly perpendicular impact at the specimen's minimum cross-section in experimental tests, which may result in slight misalignments and small impact angles. Possible rotation of the steel spheres, potentially induced by friction within the air-gun barrel, may also have contributed to the observed discrepancies by introducing small local tangential speed components at contact and causing slight deviations in the impact point or locally asymmetric deformation. Although the barrel used in the setup is specifically sized for the projectile diameter, it is reasonable to assume that friction could generate residual spin and thereby indirectly enhance any minor misalignment already present in the experimental configuration. Evidence of non-ideal impact conditions can be seen, for example, in Fig. 6b and l, where the dent geometries are not symmetric with respect to the plane which contains the specimen axis and the impact direction. Furthermore, dimension h is smaller than the other two and more susceptible to measurement errors, as it represents a depth parameter that is difficult to assess with the microscope. In the experimental tests, h was measured from a point located near the dent rim as reference, due to the difficulty of identifying a common reference point on the specimen surface under the lens. In contrast, in the finite element analyses, the maximum displacement in the specimen at the end of the simulation was

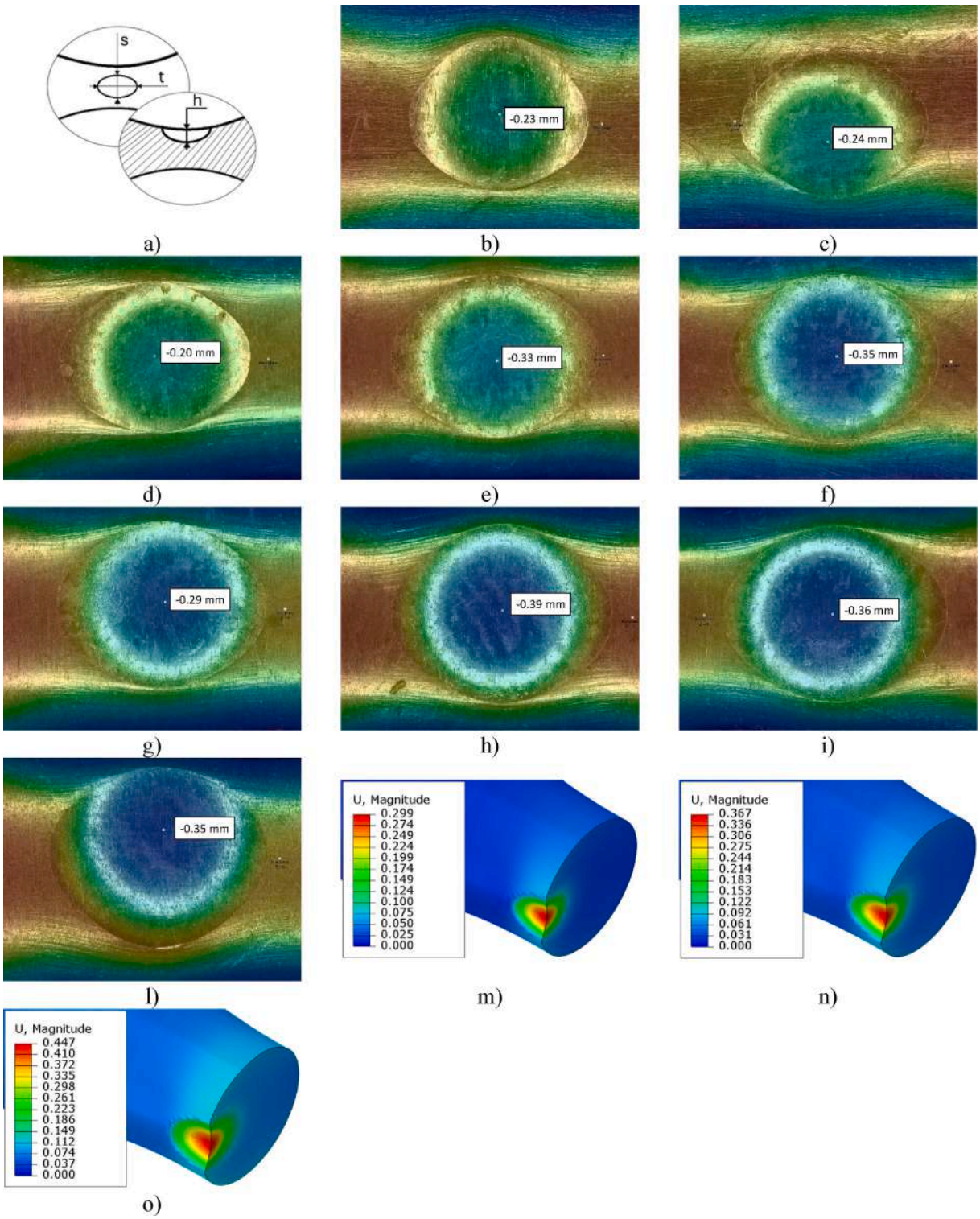

Fig. 6. Impact dent dimensions: a) definition of the dimensions; (b-l: experimental results) b) Specimen 1; c) Specimen 2; d) Specimen 3; e) Specimen 4; f) Specimen 5; g) Specimen 6; h) Specimen 7; i) Specimen 8; l) Specimen 9; (m-o: finite element results, displacement in mm); m) impact speed: 75 m/s; n) impact speed: 87.5 m/s; o) impact speed: 100 m/s.

assumed to be the h dimension. Overall, these results confirm that the finite element model provides an accurate representation of the impact dent geometry and can therefore be considered sufficiently validated for use in the subsequent stress-analysis phase.

3.2. Experimental fatigue results and finite element analysis of stress evolution

The number of cycles to failure for each specimen tested under rotating bending fatigue is reported in Table 4, along with the corresponding impact speeds.

The number of cycles to failure showed limited variation within each

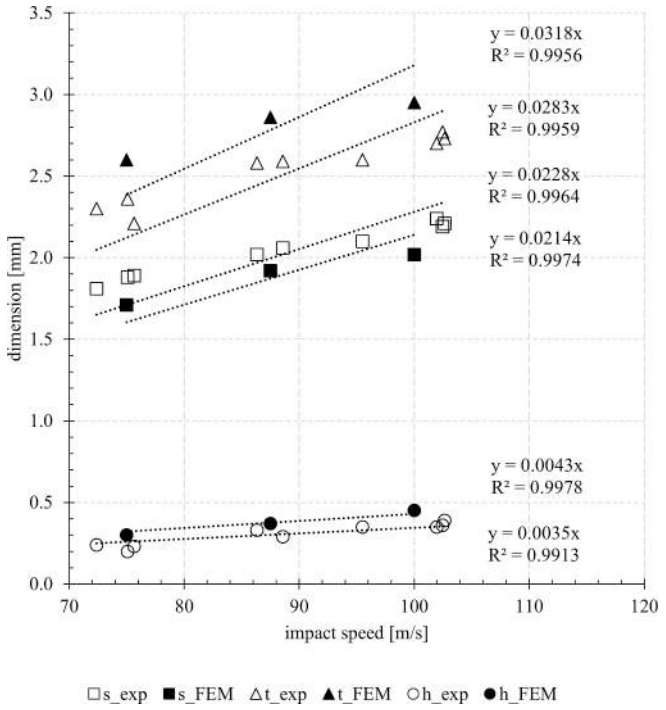

Fig. 7. Impact dent dimension trends, both for experimental and finite element results.

Table 4
Cycles to failure for the different tested specimens.

Specimen	Speed [m/s] nominal	Measured	Number of cycles to failure
1	75.0	75.66	32,052
2		72.39	36,791
3		75.09	38,069
4	87.5	86.34	34,032
5		95.51	42,511
6		88.59	36,642
7	100.0	102.64	61,454
8		102.46	33,052
9		101.96	44,789

impact speed group and across the overall dataset. The consistency of the three repeated measurements performed at each impact-speed level could, in principle, be assessed using the Grubbs outlier test with a significance level of 0.05, even though the sample size is small. If such a test were conducted, the calculated statistics would remain below the corresponding critical threshold for all groups, indicating that the measured fatigue lives would be statistically consistent and that no significant outliers would be identified. However, since Specimen 7 reached nearly twice the cycle count of the other specimens, it was excluded from the analysis. The remaining data were considered reliable and used for further evaluation. Fig. 8 presents the results as a plot of measured impact speed versus cycles to failure, with the cycle axis shown on a base-10 logarithmic scale. The trend line appears nearly horizontal, indicating that the tested impact speed has minimal influence on fatigue resistance within the investigated range. However, a very low value of R^2 was obtained.

Fig. 9 presents the fracture surfaces of the 7075-T6 hourglass specimens after rotating bending fatigue, arranged by increasing impact speed. Subfigures a–c refer to the nominal impact speed of 75 m/s, d–f to 87.5 m/s, and g–i to 100 m/s. All specimens exhibit the three classical regions of fatigue failure: the crack initiation site, the stable crack propagation zone, and the final overload region. Despite the different impact speeds, the overall morphology of the fracture surfaces remains remarkably consistent. In every specimen, the fatigue crack initiated at or very close to the root of the impact dent, where tensile stresses are expected to occur. This shows that the impact crater acts as a severe stress concentrator and that the local residual stress field promotes crack nucleation at the dent rim. Following initiation, a smooth region of stable crack propagation extends from the dent root. This zone displays characteristic fatigue patterns and remains relatively uniform across all impact conditions. Specimens impacted at 75 m/s show a well-defined initiation area and a broad, smooth propagation region, indicative of stable crack growth. At 87.5 m/s, the initiation zone appears slightly more extended, consistent with the marginally deeper dent geometry, although the propagation morphology remains comparable. For specimens impacted at 100 m/s, the initiation site is again located at the dent rim, and the transition from initiation to propagation appears more abrupt, likely due to the more severe local deformation induced by the higher-energy impact. Nevertheless, the size and texture of the propagation region do not exhibit significant enlargement relative to lower-speed impacts. The final overload region occupies a similar fraction of the fracture surface across all specimens. This region reflects rapid failure once the remaining cross-section could no longer sustain the applied bending moment. The relative proportions of the propagation

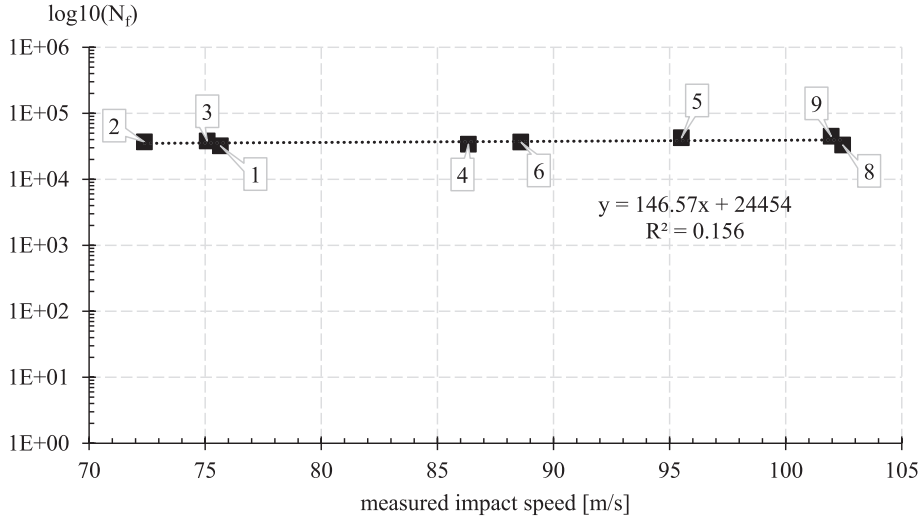

Fig. 8. Measured impact speed versus cycles to failure graph.

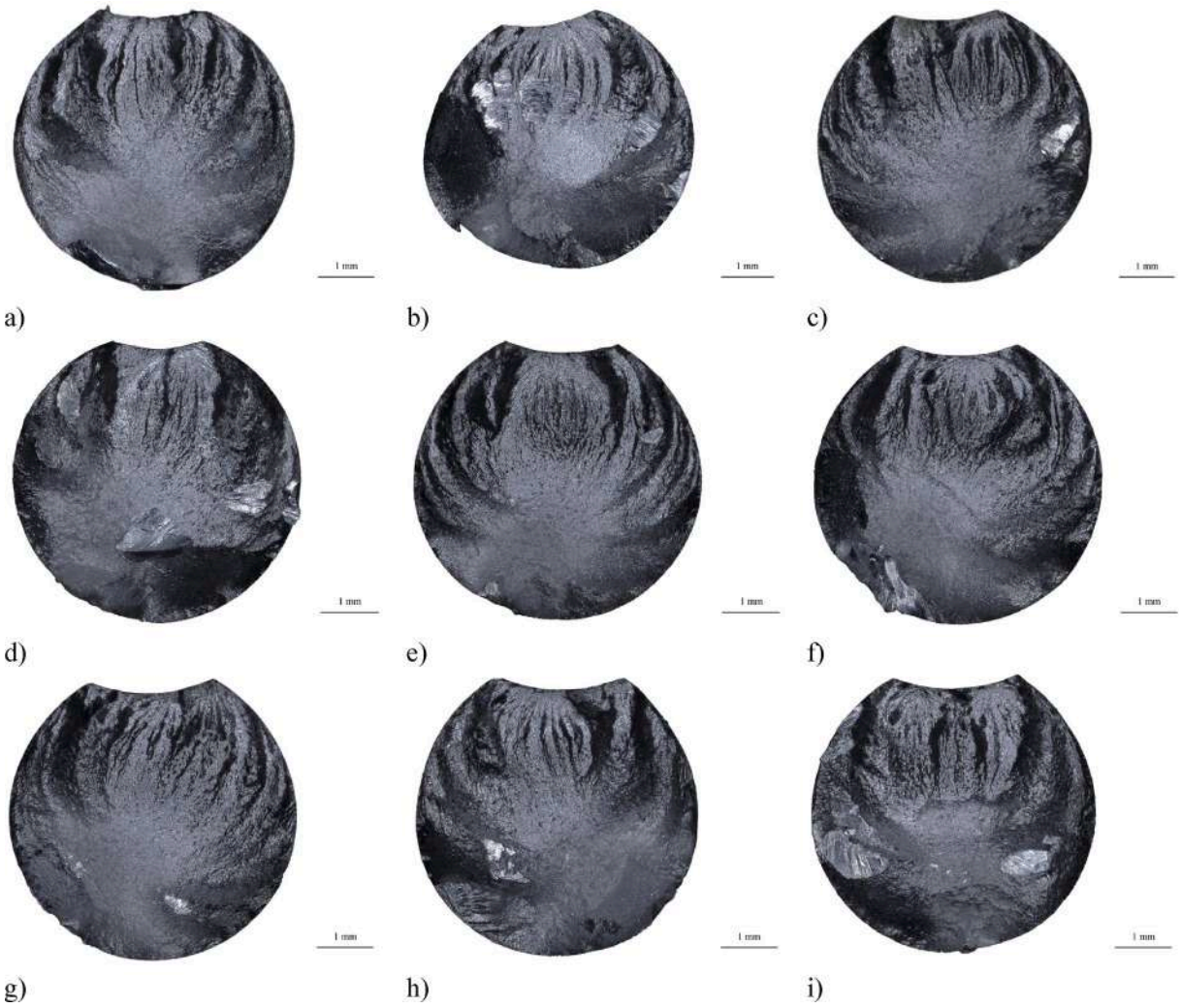

Fig. 9. Fracture surfaces of the tested specimens: a) Specimen 1; b) Specimen 2; c) Specimen 3; d) Specimen 4; e) Specimen 5; f) Specimen 6; g) Specimen 7; h) Specimen 8; i) Specimen 9.

and overload zones remain essentially unchanged with increasing impact speed, supporting the experimental fatigue-life results, which showed no significant reduction in life as impact speed increased from 75 to 100 m/s. This morphological consistency indicates that, within the investigated speed range, the severity of the notch effect and the associated residual stress field are similar among the specimens, leading to a fatigue failure mechanism governed primarily by the local stress state at the dent root. Although the fracture morphology of all tested specimens is similar, an exception is represented by Specimen 7 (Fig. 9g), which exhibits a pronounced deviation from the expected symmetry of the failure surface. This atypical pattern suggests a non-representative failure mechanism, likely influenced by local microstructural or geometric irregularities. This observation further supports its exclusion from the fatigue-life analysis. Overall, the fracture surface analysis confirms that the impact speed does not significantly alter the fatigue failure mechanism of the specimens: crack initiation is consistently controlled by the dent geometry and local stress state, while the subsequent propagation behavior remains largely unaffected by the impact speed.

Residual axial stresses after impact, obtained from the finite element calculation, are shown in Fig. 10, with subfigures a, b, and c corresponding to impact speeds of 75 m/s, 87.5 m/s, and 100 m/s, respectively. In all cases, the stress distribution remains qualitatively similar: the area close to the impact dent is subjected to tensile stresses while the area between the specimen center and the impact dent to compressive stresses.

Fig. 11 summarizes the axial stress evolution in the damaged specimens during the two simulated rotating bending cycles, i.e., with the angular position of the concentrated force ranging from 0° to 720°. The angular position 0° corresponds to the concentrated force applied along the impact direction, towards the impacting sphere, so that the impact dent is subjected to tensile bending stresses. Subfigures a, c and e show the stress distributions when the maximum tensile stress occurs, while subfigures b, d and f show the stress evolution at the points of the specimen where the maximum stress amplitude, mean stress and peak stresses occur. These three configurations are analyzed as representative. All the points are located on or near the impact dent surface. For the impact case with speed of 75 m/s, the positions of the points of maximum mean stress and maximum peak stress do not coincide. However, the differences in mean stress and stress amplitude between the two points are only a few MPa, and the stress evolution is almost identical. For the other two impact cases, the location of the point with maximum tensile stress coincides with that of the maximum mean stress. These results highlight therefore the marked contribution of the residual stresses to the total stresses during rotating bending loading.

Table 5 reports the mean stresses and stress amplitudes for the stress evolutions shown in Fig. 11b, d and f, corresponding to the points of maximum stress amplitude, mean stress, and peak stress. The last rows of the table list the ratios between the stress values for each impact speed and the corresponding value for the preceding speed. The ratios between

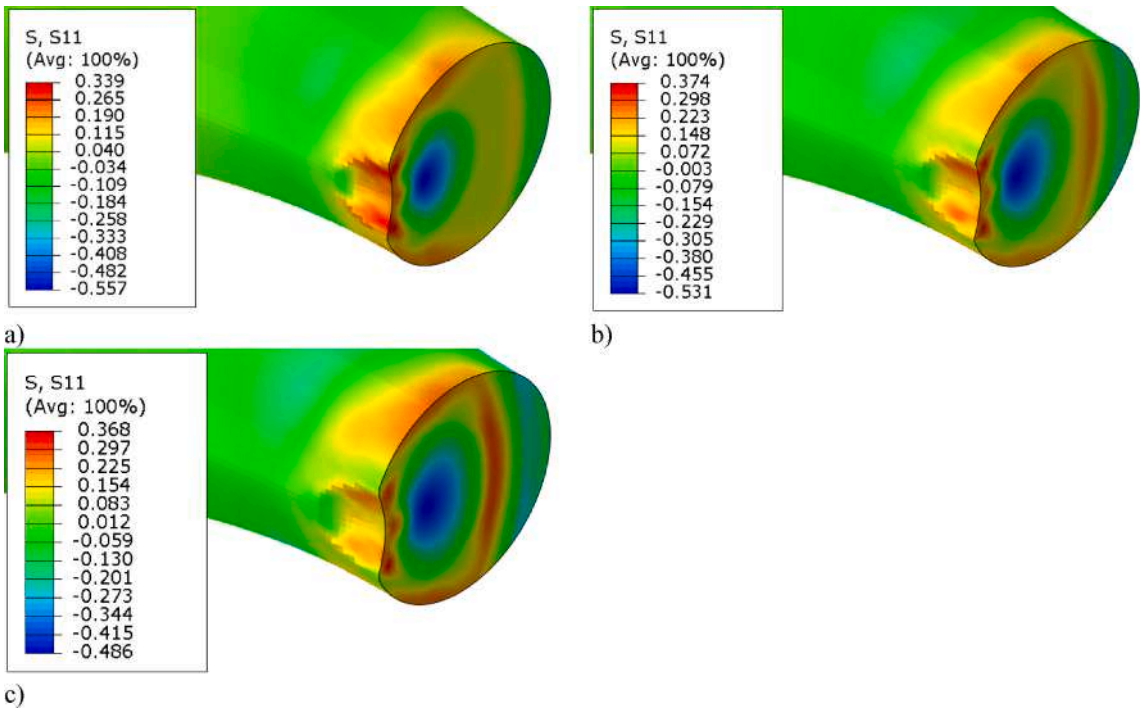

Fig. 10. Axial stresses in the specimens (in GPa): a) impact speed = 75 m/s; b) impact speed = 87.5 m/s; c) impact speed = 100 m/s.

the 75 and 87.5 m/s cases, as well as those between 87.5 and 100 m/s, are generally close to 100%. The only exception is represented by the ratio between the 75 and 87.5 m/s cases when considering the points of maximum stress amplitude. For these points, the stress curves at the intermediate and higher impact speeds show that compressive stresses develop during part of the rotating-bending cycle, which is beneficial from a fatigue viewpoint. Neglecting this specific case, the other ratios can explain why the experiments provided similar results across the three impact speeds.

The evolution of stresses during the fatigue cycles is strongly influenced by the residual stress state, which is similar among the three specimens, as shown in Fig. 10. Under rotating bending conditions, the applied load generates tensile bending stresses that reach their maximum at the specimen surface. When residual stresses are present, the total stress distribution results from the superposition of these bending stresses and the residual stresses, which can either mitigate or amplify the stress level. This interaction explains why shot peening is widely used to enhance the fatigue strength of metallic components. Shot peening produces very high compressive residual stresses within the first approximately 100 μm below the surface, effectively reducing the total surface stress by counteracting the tensile bending stresses. As a consequence, surface crack initiation is suppressed and cracks tend to initiate in subsurface areas, typically at inclusions, which are less critical under pure rotating bending conditions [52]. Although both shot peening and single-impact loading induce residual stresses, the nature and extent of the resulting fields differ substantially. Shot peening generates a broad, uniform compressive layer over the treated surface, whereas a single impact produces a highly localized compressive zone confined to the vicinity of the dent. To satisfy equilibrium condition, this localized compression is accompanied by tensile residual stresses in adjacent regions. In the analyzed impact damaged hourglass specimens, tensile residual stresses appear at the surface (see red areas in Fig. 10). In this region, the bending stresses reach their maximum during rotating bending and the total stress at the surface, given by the superposition of bending stress and tensile residual stress, consequently becomes higher than the bending stress alone. These tensile zones represent a concern for fatigue performance and help explain why the single impact does not provide the beneficial effect typically associated with shot peening.

Material yielding was observed to occur and extend in some areas of the impact-damaged specimens under rotating bending, as shown in Fig. 12, which reports the plastic strain at the end of the first and second simulated cycles. This can explain the small differences in stress evolution between the two subsequent cycles reported in Fig. 11. Accordingly, the values in Table 5 are calculated considering the maximum and minimum stresses over the two cycles. The obtained plastic strains are small and do not significantly affect the stress histories over the first two cycles; however, their presence and progressive extension indicate that fatigue damage may be governed by strain-controlled mechanisms over the full fatigue life. For this reason, future studies could incorporate strain-based criteria [53] or combined stress–strain approaches such as critical plane methods [54]. Crack propagation, which is not analyzed in the present study, could be addressed through fracture mechanics approaches. Since the stress evolutions during the first two cycles obtained from the finite element analyses are very similar for all impact speeds, it is reasonable to assume that the stress–strain state evolves in a similar manner throughout the fatigue life. This provides a consistent explanation for the comparable fatigue lives observed experimentally across the different impact conditions, even if strain-based approaches were not used in the analysis and material failure was not modelled.

To sum up, experimental and finite element results suggest that, in the tested range, the influence of impact speed on fatigue behavior remains limited. These findings are noteworthy even though the simulation was restricted to two rotating bending cycles and crack initiation and propagation phenomena were not modelled. Finally, all results are based solely on the analysis of axial stress components. However, the actual stress state beneath the impact dent is triaxial. For a more comprehensive and accurate assessment of fatigue behavior, multiaxial fatigue criteria could be adopted.

4. Conclusions

This study experimentally and numerically investigated the fatigue behavior of 7075-T6 hourglass specimens subjected to perpendicular impact damage at speeds ranging from 75 to 100 m/s at the minimum

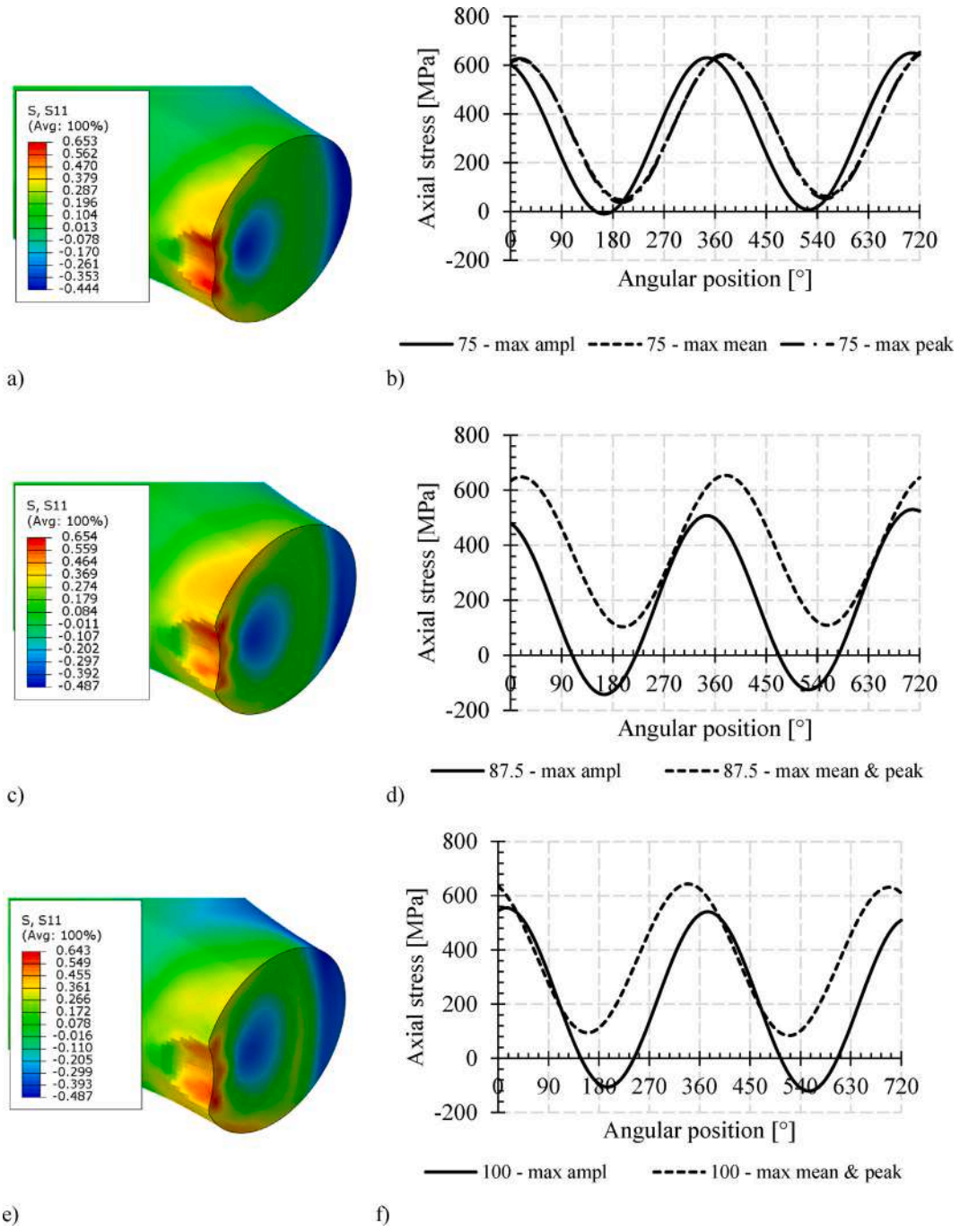

Fig. 11. Axial stresses under rotating bending: a) stress distribution in the specimen damaged at 75 m/s when the maximum tensile stress occurs (stresses in GPa); b) stress evolution in the points of the specimen damaged at 75 m/s where the maximum stress amplitude, mean stress and peak stress occur; c) stress distribution in the specimen damaged at 87.5 m/s when the maximum tensile stress occurs (stresses in GPa); d) stress evolution in the points of the specimen damaged at 87.5 m/s where the maximum stress amplitude, mean stress and peak stress occur; e) stress distribution in the specimen damaged at 100 m/s when the maximum tensile stress occurs (stresses in GPa); f) stress evolution in the points of the specimen damaged at 100 m/s where the maximum stress amplitude, mean stress and peak stress occur.

Table 5
Mean stress and stress amplitude at the points of the damaged specimens where the maximum stress amplitude, mean stress and peak stress occur.

Impact speed [m/s]	75			87.5		100	
Point	max amplitude	max mean	max peak	max amplitude	max mean & peak	max amplitude	max mean & peak
Mean stress [MPa]	320	347	345	193	379	217	364
Stress amplitude [MPa]	330	299	308	336	275	337	279
Ratios	mean			60%	109%	112%	96%
	amplitude			102%	92%	100%	101%

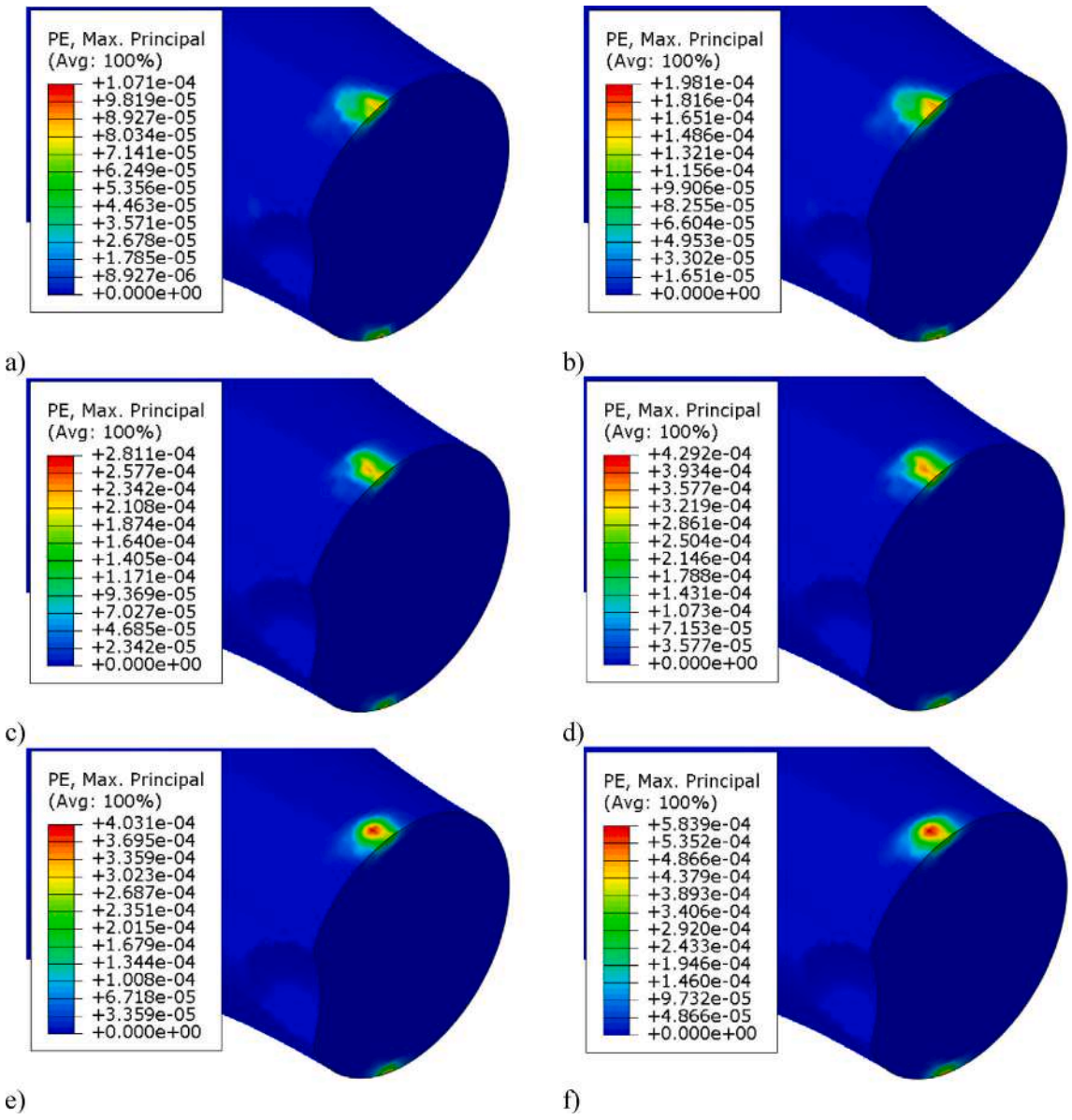

Fig. 12. Maximum principal plastic strain: a) impact speed: 75 m/s, end of the first simulated cycle; b) impact speed: 75 m/s, end of the second simulated cycle; c) impact speed: 87.5 m/s, end of the first simulated cycle; d) impact speed: 87.5 m/s, end of the second simulated cycle; e) impact speed: 100 m/s, end of the first simulated cycle; f) impact speed: 100 m/s, end of the second simulated cycle.

cross section. In the finite element analyses for impact simulation, the strain-rate dependency of the material properties was taken into account using Johnson-Cook model. The results showed that the geometry of the impact dent varies linearly with impact speed. Although finite element analyses slightly overestimated dent depth compared to experiments, the obtained discrepancies are within acceptable limits. The number of cycles to failure obtained from the rotating-bending tests fell within a narrow range of 30,000–45,000 cycles for all impact conditions, indicating that impact speed had a limited influence on fatigue life within the considered impact conditions. Crack initiation occurred at the dent root, and the morphology of the propagation and overload regions was similar for all the tested specimens, confirming that the fatigue failure mechanism is largely unaffected by impact speed. Finite element analyses showed that the tensile residual stresses at the dent rim significantly contribute to the total surface stress during cyclic loading. The residual stress fields generated at the three impact speeds were qualitatively similar, explaining the comparable fatigue lives. The superposition of residual and applied bending stresses produced nearly identical stress histories at the critical points for all impact conditions, supporting the experimental observation of similar fatigue performance. Small plastic strains were observed during the first two simulated cycles, suggesting that strain-controlled mechanisms may contribute to long-term fatigue damage. Overall, the combined experimental and numerical evidence demonstrates that, within the investigated range, impact speed does not significantly influence the residual stress field and the stress evolution under rotating bending loading.

CRediT authorship contribution statement

Emanuele Vincenzo Arcieri: Writing – original draft, Resources, Methodology, Investigation, Formal analysis, Data curation, Conceptualization. **Sergio Baragetti:** Writing – review & editing, Visualization, Validation, Supervision, Resources, Methodology, Investigation, Conceptualization. **Željko Božić:** Writing – review & editing, Visualization, Validation, Supervision.

Declaration of competing interest

The authors declare that they have no known competing financial interests or personal relationships that could have appeared to influence the work reported in this paper.

Acknowledgements

The authors wish to thank Daniele Colombi for his help.

Appendix A. Supplementary data

Supplementary data to this article can be found online at https://doi.org/10.1016/j.ijfatigue.2026.109602.

Data availability

Data will be made available on request.

References

[1] Nicholas T. Foreign object damage. In: Suresh S, editor. High Cycle Fatigue. Oxford: Elsevier; 2006. p. 322–76. https://doi.org/10.1016/B978-008044691-2/50007-2.
[2] Peters JO, Roder O, Boyce BL, Thompson AW, Ritchie RO. Role of foreign-object damage on thresholds for high-cycle fatigue in Ti-6Al-4V. Metall Mater Trans A 2000;31:1571–83. https://doi.org/10.1007/s11661-000-0167-2.
[3] Fleury RMN, Nowell D. Evaluating the influence of residual stresses and surface damage on fatigue life of nickel superalloys. Int J Fatigue 2017;105:27–33. https://doi.org/10.1016/j.ijfatigue.2017.08.015.
[4] Boyce BL, Chen X, Hutchinson JW, Ritchie RO. The residual stress state due to a spherical hard-body impact. Mech Mater 2001;33:441–54. https://doi.org/10.1016/S0167-6636(01)00064-3.
[5] Peters JO, Ritchie RO. Influence of foreign-object damage on crack initiation and early crack growth during high-cycle fatigue of Ti–6Al–4V. Eng Fract Mech 2000;67:193–207. https://doi.org/10.1016/S0013-7944(00)00045-X.
[6] Božić Ž, Schmauder S, Mlikota M. Fatigue growth models for multiple long cracks in plates under cyclic tension based on ΔKI, ΔJ-integral and ΔCTOD parameter. Key Eng Mater 2012;488–489:525–8. https://doi.org/10.4028/www.scientific.net/KEM.488-489.525.
[7] Calvo-García E, Barro Ó, Pou-Álvarez P, Badaoui A, Wallerstein D, Riveiro A, et al. Fatigue crack growth and fracture toughness of shot peened 6060 T6 aluminium alloy. Procedia Struct Integr 2025;68:809–14. https://doi.org/10.1016/j.prostr.2025.06.134.
[8] Mlikota M, Schmauder S, Dogahe K, Božić Ž. Influence of local residual stresses on fatigue crack initiation. Procedia Struct Integr 2021;31:3–7. https://doi.org/10.1016/j.prostr.2021.03.002.
[9] Baragetti S, Tordini F. Fatigue resistance of PECVD coated steel alloy. Int J Fatigue 2007;29:1832–8. https://doi.org/10.1016/j.ijfatigue.2007.02.008.
[10] Xiaozhou F, Xiufang W, Changwei Z, Jianmin Z. Mechanical model and numerical simulation of composite laminates subjected to low velocity impact. J Phys Conf Ser 2021;2133:012008. https://doi.org/10.1088/1742-6596/2133/1/012008.
[11] Sun XC, Hallet SR. Barely visible impact damage in scaled composite laminates: Experiments and numerical simulation. Int J Impact Eng 2017;109:178–95. https://doi.org/10.1016/j.ijimpeng.2017.06.008.
[12] Riccio A, Di Felice G, La Manna G, Antonucci E, Caputo F, Lopestro V, et al. A global-local numerical model for the prediction of impact induced damage in composite laminates. Appl Compos Mater 2014;21:457–66. https://doi.org/10.1007/s10443-013-9343-6.
[13] Chen Y, Li F, Liu Y, Yi J, Fang D, Li C, et al. Impact resistance behaviors of boride reinforced Ti-6Al-4V functionally graded materials: Experimental and numerical analysis. J Alloy Compd 2024;997:174866. https://doi.org/10.1016/j.jallcom.2024.174866.
[14] Zhu S, Peng W, Shao Y, Li S. Experimental and numerical study on the high-velocity hail impact performance of carbon fiber aluminum alloy laminates. Int J Impact Eng 2023;179:104664. https://doi.org/10.1016/j.ijimpeng.2023.104664.
[15] Zhang H, Hu D, Ye X, Chen X, He Y, Ma X. Prediction on aeroengine blade foreign object damage validated by air gun tests. Eng Fail Anal 2022;143:106919. https://doi.org/10.1016/j.engfailanal.2022.106919.
[16] Yin W, Liu Y, He X, Li H. Effects of different materials on residual stress fields of blade damaged by foreign objects. Materials 2023;16:3662. https://doi.org/10.3390/ma16103662.
[17] Li Z, Zhang T, Zhang H, Zhao Z. Research on the damage characteristics of Ti-6Al-4V simulation blades subjected to foreign object damage. Shock Vib 2024;2024:6020692. https://doi.org/10.1155/2024/6020692.
[18] Zhang H, Hu D, Ye X, Chen X, He Y. Experimental and analytical modelling on aeroengine blade foreign object damage. Int J Impact Eng 2024;183:104813. https://doi.org/10.1016/j.ijimpeng.2023.104813.
[19] Duò P, Liu J, Dini D, Golshan M, Korsunsky AM. Evaluation and analysis of residual stresses due to foreign object damage. Mech Mater 2007;39:199–211. https://doi.org/10.1016/j.mechmat.2006.05.003.
[20] Frankel PG, Withers PJ, Preuss M, Wang H-T, Tong J, Rugg D. Residual stress fields after FOD impact on flat and aerofoil-shaped leading edges. Mech Mater 2012;55:130–45. https://doi.org/10.1016/j.mechmat.2012.08.007.
[21] Yang W, Yang H, Liu J, Zeng Y, Wang X, Li L. Foreign object damage characteristics of a thin nickel-based superalloy plate at room and high temperatures. Thin-Walled Struct 2024;202:112065. https://doi.org/10.1016/j.tws.2024.112065.
[22] Nowell D, Duò P, Stewart IF. Prediction of fatigue performance in gas turbine blades after foreign object damage. Int J Fatigue 2003;25:963–9. https://doi.org/10.1016/S0142-1123(03)00160-9.
[23] Arcieri EV, Baragetti S, Bozic Z. Residual stress modelling and analysis of a 7075-T6 hourglass specimen after foreign object damage. Procedia Struct Integr 2023;46:24–9. https://doi.org/10.1016/j.prostr.2023.06.005.
[24] Oakley SY, Nowell D. Prediction of the combined high- and low-cycle fatigue performance of gas turbine blades after foreign object damage. Int J Fatigue 2007;29:69–80. https://doi.org/10.1016/j.ijfatigue.2006.02.042.
[25] Zhu L, Hu X, Jiang R, Song Y, Qu S. Experimental investigation of small fatigue crack growth due to foreign object damage in titanium alloy TC4. Mater Sci Eng A 2019;739:214–24. https://doi.org/10.1016/j.msea.2018.10.031.
[26] Ding J, Hall RF, Byrne J, Tong J. Fatigue crack growth from foreign object damage under combined low and high cycle loading. Part I: Experimental studies. Int J Fatigue 2007;29:1339–49. https://doi.org/10.1016/j.ijfatigue.2006.10.020.
[27] Ding J, Hall RF, Byrne J, Tong J. Fatigue crack growth from foreign object damage under combined low and high cycle loading. Part II: a two-parameter predictive approach. Int J Fatigue 2007;29:1350–8. https://doi.org/10.1016/j.ijfatigue.2006.10.014.
[28] Yin W, Liu Y, He X, Tian Z. High-cycle fatigue strength prediction model for Ti-6Al-4V titanium alloy compressor blades subjected to foreign object damage. Metals 2025;15:1150. https://doi.org/10.3390/met15101150.
[29] Zhang T, Lu K, Wang L, Zhao Z, Zheng G. Effect of foreign object damage on the fatigue performance of stainless steel blades under pre-corrosion conditions. Metals 2025;15:357. https://doi.org/10.3390/met15040357.
[30] Majumdar S, Sinha A, Das A, Datta P, Nag D. An insight view of evolution of advanced aluminum alloy for aerospace and automotive industry: current status and future prospects. J Inst Eng India Ser D 2024. https://doi.org/10.1007/s40033-024-00852-z.
[31] Baragetti S, Villa F. Corrosion fatigue of high-strength titanium alloys under different stress gradients. JOM 2015;67:1154–61. https://doi.org/10.1007/s11837-015-1360-5.
[32] Eylon D, Fujishiro S, Postans PJ, Froes FH. High-Temperature Titanium Alloys—A Review. JOM 1984;36:55–62. https://doi.org/10.1007/BF03338617.
[33] Li SS, Yue X, Li QY, Peng HL, Dong BX, Liu TS, et al. Development and applications of aluminum alloys for aerospace industry. J Mater Res Technol 2023;27:944–83. https://doi.org/10.1016/j.jmrt.2023.09.274.
[34] Arcieri EV, Baragetti S, Lavella M. Effects of FOD on fatigue strength of 7075-T6 hourglass specimens. IOP Conf Ser: Mater Sci Eng 2021;1038:012012. https://doi.org/10.1088/1757-899X/1038/1/012012.
[35] Arcieri EV, Baragetti S, Božić Ž. Stress assessment and fracture surface analysis in a foreign object damaged 7075-T6 specimen under rotating bending. Eng Fail Anal 2022;138:106380. https://doi.org/10.1016/j.engfailanal.2022.106380.
[36] Arcieri EV, Baragetti S. Cyclic loading on damaged AA7075-T6 specimens: Numerical modelling and experimental testing. J Multiscale Model 2022;13:2144005. https://doi.org/10.1142/S1756973721440054.
[37] Arcieri EV, Baragetti S, Bozic Z. Application of design of experiments to foreign object damage on 7075-T6. Procedia Struct Integr 2021;31:22–7. https://doi.org/10.1016/j.prostr.2021.03.005.
[38] Arcieri EV, Baragetti S. Finite element and design of experiments study on stresses in impact-damaged hourglass specimens subjected to rotating bending. J Multiscale Model 2024;15:2441001. https://doi.org/10.1142/S1756973724410014.
[39] Arcieri EV, Baragetti S, Božić Ž. Numerical analysis of impact damage at different impact speeds. Procedia Struct Integr 2025;68:1324–8. https://doi.org/10.1016/j.prostr.2025.06.206.
[40] Colombi D. Analisi della resistenza a fatica di provini a clessidra in alluminio 7075-T6 soggetti a danneggiamento da impatto: studi numerici e prove sperimentali. Master thesis: 2024.
[41] Askari-paykani M, Meratian M, Shanay M, Raeissi K. Effects of heat treatment parameters on microstructural changes and corrosion behavior of Al 7075 Alclad alloy. Anti-Corros Methods Mater 2012;59:231–8. https://doi.org/10.1108/00035591211265523.
[42] Louhinchi MA, Poulanchon G, Lorong P, Do Outeiro JCM, Monteiro E, Cotton D. Modeling and validation of residual stresses induced by heat treatment of AA 7075-T6 samples toward the prediction of part distortion. Mach Sci Technol 2023;27:247–67. https://doi.org/10.1080/10910344.2023.2215309.
[43] Baragetti S, Borzini E, Bozic Z, Arcieri EV. On the fatigue strength of uncoated and DLC coated 7075-T6 aluminum alloy. Eng Fail Anal 2019;102:219–25. https://doi.org/10.1016/j.engfailanal.2019.04.035.
[44] ISO 1143:2021, Metallic materials – Rotating bar bending fatigue testing.
[45] Davoli P, Vergani L, Beretta S, Guagliano M, Baragetti S. Costruzione di macchine 1. 2nd ed. Milano: Mc-Graw-Hill; 2007.
[46] Abaqus 2022. Dassault Systèmes.
[47] Farahani HK, Ketabchi M, Zangeneh S. Determination of Johnson–Cook plasticity model parameters for Inconel718. J Mater Eng Perform 2017;26:5284–93. https://doi.org/10.1007/s11665-017-2990-2.

[48] Shah IA, Khan R, Koloor SSR, Petrù M, Badshah S, Ahmad S, et al. Finite element analysis of the ballistic impact on auxetic sandwich composite human body armor. Materials 2022;15:2064. https://doi.org/10.3390/ma15062064.
[49] Banerjee A, Dhar S, Acharyya S, Datta D, Nayak N. Determination of Johnson Cook material and failure model constants and numerical modelling of Charpy impact test of armour steel. Mater Sci Eng A 2015;640:200–9. https://doi.org/10.1016/j.msea.2015.05.073.
[50] Friction-Coefficients for Common Materials and Surfaces. Available online: https://www.engineeringtoolbox.com/friction-coefficients-d_778.html.
[51] Lee HW, Basaran C. A review of damage, void evolution, and fatigue life prediction models. Metals 2021;11:609. https://doi.org/10.3390/met11040609.
[52] Lepitre P, Merlet LM, Doudard C, Dhondt M, Surand M, Calloch S. Influence of shot-peening on the self-heating behavior and fatigue properties of 300M steel. Mech Mater 2024;199:105174. https://doi.org/10.1016/j.mechmat.2024.105174.
[53] Basan R, Marohnić T, Božić Ž, Marković E. Investigation of methods for estimation of fatigue parameters and behavior of aluminum and titanium alloys. Procedia Struct Integr 2025;68:782–7. https://doi.org/10.1016/j.prostr.2025.06.130.
[54] Fatemi A, Socie DF. A critical plane approach to multiaxial fatigue damage including out-of-phase loading. Fatigue Fract Eng Mater Struct 1998;11:149–65. https://doi.org/10.1111/j.1460-2695.1988.tb01169.x.